High-strain-rate deformation and comminution of silicon carbide

C. J. Shih

Institute for Mechanics and Materials and Department of Applied Mechanics and Engineering Sciences, University of California, San Diego, La Jolla, California 92093

V. F. Nesterenko

Department of Applied Mechanics and Engineering Sciences, University of California, San Diego, La Jolla, California 92093

M. A. Meyers[a)]

Institute for Mechanics and Materials and Department of Applied Mechanics and Engineering Sciences, University of California, San Diego, La Jolla, California 92093

Granular flow of comminuted ceramics governs the resistance for penetration of ceramic armor under impact. To understand the mechanism of the granular flow, silicon carbide was subjected to high-strain, high-strain-rate deformation by radial symmetric collapse of a thick-walled cylinder by explosive. The deformation, under compressive stresses, was carried out in two stages: the first stage prefractured the ceramic, while a large deformation was accomplished in the second stage. The total tangential strain (-0.23) was accommodated by both homogeneous deformation (-0.10) and shear localization (-0.13). Three microstructures, produced by different processing methods, were investigated. The microstructural differences affected the microcrack propagation: either intergranular or transgranular fracture was observed, depending on the processing conditions. Nevertheless, the spacing between shear bands and the shear displacement within the shear bands were not significantly affected by the microstructure. Within the shear bands, the phenomenon of comminution occurred, and the thickness of the shear bands increased gradually with the shear strain. A bimodal distribution of fragments developed inside the shear bands. The comminution proceeded through the incorporation of fragments from the shear-band interfaces and the erosion of fragments inside the shear band. Outside the shear bands, an additional comminution mechanism was identified: localized bending generated comminution fronts, which transformed the fractured material into the comminuted material. The observed features of high-strain-rate deformation of comminuted SiC can be used for validation of computer models for penetration process. © *1998 American Institute of Physics.* [S0021-8979(98)04708-2]

I. INTRODUCTION

Armor systems consist of a complex combination of materials, including a ceramic hard front face and an energy-absorbing rear face. The ceramic is used to defeat the projectile through blunting, rupture, erosion, and other dissipation processes including high-strain-rate flow of comminuted ceramics. To date, there is no strong correlation between any mechanical properties of the ceramic and the ballistic performance of the armor system. However, all good armor ceramics have high hardness, high Young's modulus, high sonic velocity, low Poissons' ratio, moderate density, and low porosity.[1] Silicon carbide (SiC) exhibits all of these attributes and is an excellent candidate as an armor ceramic.

Ceramics have been incorporated into advanced armor systems for over 20 years. The evolution of damage during ballistic impact of ceramics can be divided into four classes:[2–4] (1) formation of a comminuted zone (also known as the Mescall zone), produced by shock waves; (2) radial and conical cracks caused by radially expanding stress waves; (3) spalling generated by reflected, tensile pulses; and (4) flow of the comminuted material.

In the comminuted zone, the high-amplitude shock waves create stresses that exceed the strength of the ceramic and result in fine ceramic fragments. Recent experiments have demonstrated the presence of the comminuted zone in various ceramics subjected to rod impact.[3,5,6] In order to allow the penetrator to continue moving through the material, the comminuted zone has to flow around the penetrator, under high strain and high-strain rate. The deformation of the comminuted ceramic proceeds in a constrained volumetric condition because the surrounding material imposes a lateral confinement. Curran *et al.*[7] developed a microstructural model of a comminuted ceramic subjected to large strain and divergent flow. Inelastic deformation is described by sliding and ride-up of fragments and the competition between dilatation and compaction is included. They demonstrated that the most important ceramic properties that determine the penetration resistance of the armor ceramic are (1) the friction between comminuted granules, (2) the unconfined compressive strength of the intact material, and (3) the strength of the comminuted material. For example, a threefold in-

---

[a)]Electronic mail: mameyers@ucsd.edu

crease in intergranular friction decreases the penetration depth by a factor of 3.

Different experimental approaches have been developed to investigate the behavior of comminuted materials under high-strain, high-strain-rate conditions. Klopp and Shockey[8] used a laser doppler velocimeter system to investigate the strength of comminuted SiC at high-strain rates (10^5 s^{-1}). They obtained that the strength at this condition is essentially lower than at a quasistatic rate. The friction coefficient of 0.23 (in the Mohr–Coulomb model) from this high-strain-rate test was reported to be smaller than for quasistatic tests. Sairam and Clifton,[9] using an inclined plate impact, reported a lower internal friction at high-strain rates in granular alumina. Klopp *et al.*[10] performed a spherical cavity expansion experiment with two grades of alumina to provide high-strain-rate data to develop ceramic armor penetration models. They observed that AD-995 alumina is comminuted primarily via grain-boundary fracture and AD-85 alumina is comminuted by compaction and fracture of the intergranular glassy phase, as well as by fracture of grains of nonalpha alumina exhibiting multiple slip and by fracture of alpha grains. They used a simple model of comminution and were able to predict fragment sizes at various distances from the charge. Chen and Ravichandran[11] investigated the behavior of a glass ceramic (Macor) by imposing controlled multiaxial loading on cylindrical ceramic samples using split Hopkinson bars. The confining pressures ranged from 10 to 230 MPa under both quasistatic and dynamic loading conditions. The failure mode changes from complete fragmentation without confinement to localized brittle faulting with lateral confinement. All results[8–11] demonstrate the necessity of experiments with external stresses of 1–10 GPa, effective strains around 1, and strain rates about 10^5 s^{-1}. Dynamic measurements should be accompanied by postdeformation characterization to identify the micromechanical process of deformation, because the micromechanics of granular (comminuted) material deformation is not well established even at a qualitative level. For example, the use of the Mohr–Coulomb approach is problematic under conditions of high strain and high-strain rate, where shear localization, particle fracture, nonequilibrium heat release are involved. Experiments involving the dynamic strength measurement accompanied by postdeformation characterization under controlled conditions are necessary to develop a micromechanical model of high-strain-rate flow of comminuted material suitable for three-dimensional computer code modeling of penetration phenomena. Nesterenko *et al.*[12] showed that profuse shear localization occurs in granular alumina during large deformation under high-strain rate. Shear localization has been extensively studied for metals, but the shear localization of ceramics under high-strain-rate conditions is not yet well analyzed.

The objective of this work is to investigate the fragmentation and flow of hot-pressed silicon carbide under high-strain rate. Three different silicon carbides, with similar average grain size, were studied. Experiments were designed to examine the fragmentation and large deformation of ceramics, representing their behavior adjacent to the projectile.

II. EXPERIMENTAL PROCEDURES

A. Material and quasistatic properties

The raw material for fully dense, hot-pressed SiC is SiC powder. Because of strong covalent bonding and low diffusivity, SiC powder cannot be densified without sintering aids. Mechanical properties of hot-pressed SiC are influenced not only by its grain size but also by the grain-boundary characteristics, which are determined by the selection of sintering aids, powder blending process, and hot-pressing conditions.

Three different hot-pressed silicon carbides (designated by SiC-I, SiC-II, and SiC-III), manufactured by Cercom, Inc., were investigated in this study. Standard hot-pressing procedures were used to fabricate these materials. SiC powder was first mixed with sintering aids. The blended powder was loaded into a graphite die and then hot pressed at 2000 °C under 18 MPa. The characteristics of these three silicon carbides are described as follows.

1. SiC-I

SiC-I is a conventional SiC, using boron and carbon as sintering aids. The boron creates atomic vacancies and enhances the sintering kinetics, and the carbon removes the oxide layer, which inhibits the densification.[13,14] This type of silicon carbide has been used for various industrial applications in the last 20 years, and the material exhibits predominantly transgranular fracture under quasistatic loading, as shown in Fig. 1(a).
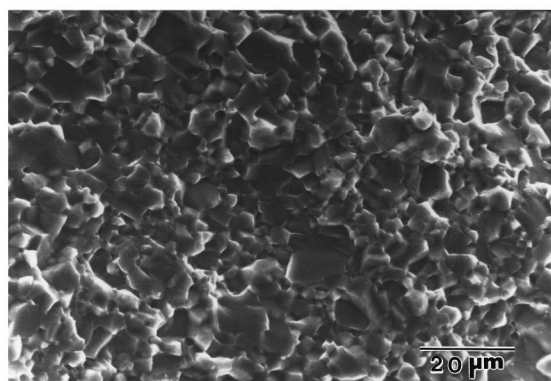
2. SiC-II

SiC-II, commercially sold as Cercom SiC-B, uses an aluminum-based compound as the sintering aid. This material has a unique microstructure: segregated grain boundaries.[15] All impurities segregate in small, well-dispersed pockets along the SiC grain boundaries. The mechanism of forming this impurity segregation is not clear yet; however, it is suspected to relate to the surface characteristics of the SiC powder. The aluminum-based sintering aid not only reacts with SiC powder to enhance diffusion but also alters the surface chemistry of SiC powder. All powder has some metallic impurities, such as iron, introduced during the powder manufacturing process. The hot-pressing temperature is around 2000 °C, which is much higher than the melting point of the metallic impurities. Metallic melts can be expected during hot pressing. Most metallic melts do not wet ceramics. During hot pressing, the coalescence of the metallic melts can result in large inclusions in the densified ceramic. These large inclusions serve as strength-limiting flaws and concomitantly affect the reliability of the ceramic. It is expected that the sintering aid promotes the wetting of the metallic melts, and allows the melts spreading over the powder surface to form fine segregated impurity pockets along the grain boundaries. These segregated impurities affect the grain-boundary characteristic distribution to promote an intergranular fracture. Intergranular fracture has been considered detrimental for metals, because it usually results in low ductility.[16,17] However, the intergranular fracture appears to be a favorable fracture mode for ceramics, because it
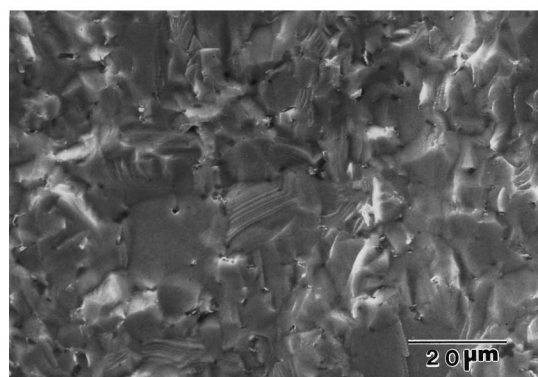
(a)
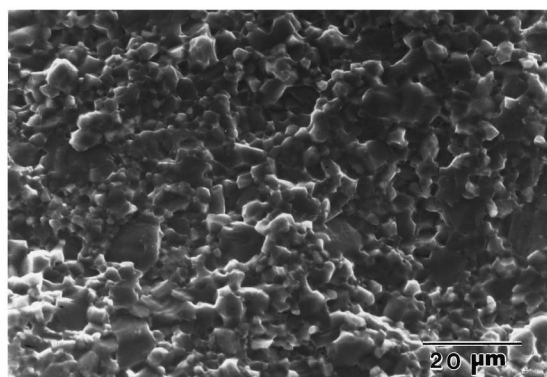
(c)

(b)

FIG. 1. Fracture surfaces of specimens after quasistatic flexural loading. (a) SiC-I, (b) SiC-II, and (c) SiC-III.

promotes crack deflection to toughen the material. As shown in Fig. 1(b), SiC-II has a predominantly intergranular fracture under quasistatic conditions.

3. SiC-III

SiC-III, commercially sold as Cercom SiC-N, is a refined product of SiC-II, with a modification in powder homogenization and an addition of organic binder. During hot pressing, the organic binder burns out and leaves a small amount of residual carbon. The extra carbon can remove the oxide layer on SiC powder. All nonoxide materials have an oxide layer. The silicon oxide layer on SiC powder may form a glassy grain-boundary phase during hot pressing, and the glassy grain-boundary phase would affect the mechanical properties of the ceramic. The difference between SiC-II and SiC-III is in the sintering aid dispersion, chemistry of the powder surface, and particle-size distribution. SiC-III also has the segregated grain boundaries, and exhibits an intergranular fracture mode under quasistatic conditions, as shown in Fig. 1(c).

Quasistatic properties of these three silicon carbides were measured from the same hot-pressed plates used to fabricate the high-strain-rate specimens, and are listed in Table I. The flexural strength was measured using the procedures outlined in ASTM C-1161 (four-point bending, using the type-B configuration), and the fracture toughness was obtained using the Chevron–Notch bending test.[18] The Weibull modulus was calculated using the maximum likelihood method on the flexural data points.[19] Elastic properties were measured using the ultrasonic technique. Average grain size was measured using an intercept method (ASTM E-112) on etched surfaces, using Murakami's reagent.

As shown in Table I, these three hot-pressed SiC had a similar average grain size. Fracture surfaces of the flexural specimens were examined. SiC-I had iron (or iron silicide) and carbon inclusions as critical, strength-limiting flaws. In contrast, processing flaws for SiC-II and SiC-III were not found. As a result, SiC-II and SiC-III had much higher flexural strength and Weibull modulus than SiC-I. SiC-II and SiC-III also had higher fracture toughness because of their segregated grain-boundary characteristics. In addition, SiC-I

TABLE I. Quasistatic properties of hot-pressed silicon carbide.

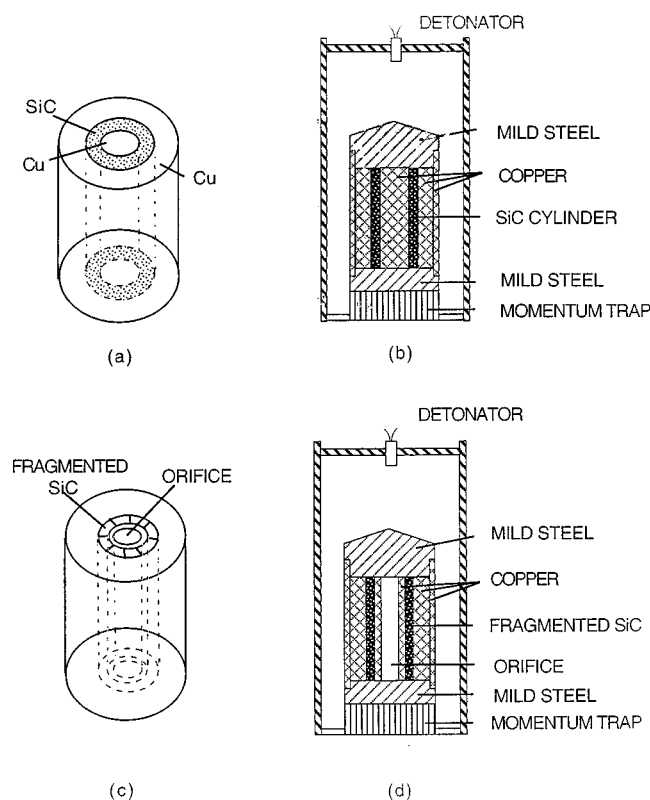|	SiC-I	SiC-II	SiC-III
Density (g/cm^3)	3.18	3.20	3.21
Average grain size (μm)	5.6	4.1	4.1
Flexural strength (MPa)	380	542	477
Weibull modulus	5.9	10.9	11.2
Fracture toughness (Mpa $\sqrt{m}$)	2.5	4.1	4.3
Hardness [Knoop 300 g] (GPa)	23.9	22.9	22.6
Young's modulus (GPa)	440	450	450
Poissons' ratio	0.17	0.17	0.17

FIG. 2. Experimental procedures: (a) specimen assembly, (b) first explosive event: fragmentation of solid ceramic, (c) orifice drilling, and (d) second explosive event: deformation of fragmented ceramic.

had a slightly higher amount of porosity, and a concomitantly lower Young's modulus.

B. High-strain-rate experiments

The thick-walled cylinder method was used to investigate the high-strain-rate deformation (3×10^4 s^{-1}) of the hot-pressed silicon carbide. Two SiC-I, three SiC-II, and two SiC-III specimens were tested under identical conditions. The experimental procedures were originally developed for metals but were modified for granular and brittle materials.[12,20–24] This method consists of two explosive events: the first event to fracture the ceramic and the second event to deform the fragmented ceramic.

The experimental steps are outlined in Fig. 2. A silicon carbide cylinder (16 mm inner diameter and 22 mm outer diameter) was assembled with a copper insert (14.5 mm diam) and a copper sleeve (23 mm inner diameter and 36 mm outer diameter). A mixture of 3:1 volume ratio of ammonite and sand was used to generate an explosion of low detonation velocity (3.2 km/s) to fracture the SiC cylinder. Detonation was initiated at the top of the charge and propagated along the cylinder axis. After this explosion, the ceramic remained cylindrical, and contained cracks and incipient shear bands.

A cylindrical orifice (11 mm diam) was then drilled in the center of the copper insert. The specimen then underwent a second explosive event using 100% ammonite to achieve a detonation velocity of 4.2–4.4 km/s to collapse the center

orifice. This explosive event produced large inelastic deformation. The objective is to simulate the flow of the fragmented ceramic under confinement. The confinement in this method is provided by the inertial compressive stresses at the boundary between the ceramic and the copper sleeve, with an amplitude less than 100 MPa.[22]

The quantitative determination of the global material strain can be obtained from the strains in the incompressible copper, i.e., the cross-sectional area of copper along the longitudinal axis remains the same during deformation.[12,22] The radial and tangential engineering strains (e_{rr} and $e_{\varphi\varphi}$) can be estimated from the initial and final radii, r_0 and r_f:

$$e_{rr} = \frac{r_0}{r_f} - 1, \quad e_{\varphi\varphi} = \frac{r_f}{r_0} - 1. \tag{1}$$

The deformation at the inner and outer radii can be measured as a function of time to calculate the strain rate during testing.[12]

III. RESULTS AND DISCUSSION

The overview of the ceramic specimens after the first and second explosive events is shown in Fig. 3. After the first explosive event, all specimens had numerous cracks and incipient shear bands. The second explosive event produced significant shear-band displacements; however, the number of the shear bands did not increase.

The total tangential strain (e_t) can be partitioned into homogeneous strain (e_h) and shear-band strain (e_s):

$$e_t = e_h + e_s. \tag{2}$$

Since the tangential strain varies from the inner radius to the outer radius, the total tangential strain is approximated at the middle point of the ceramic; i.e.,

$$e_t = \frac{r_{mf}}{r_{mo}} - 1, \tag{3}$$

where r_{mo} and r_{mf} are the initial and final mean radii, respectively. The strain due to shear localization is obtained by taking the tangential component of the shear-band displacement [$(\sqrt{2}/2)\Delta$] through the following equation (Δ is shown in Fig. 3):

$$e_s = -\frac{\sqrt{2}\Sigma\Delta}{4\pi r_{mo}}, \tag{4}$$

where $\Sigma\Delta$ is the summation of all shear-band displacements.

The tangential strain after these two explosive events is listed in Tables II and III. The total tangential strain (e_t) for these three different silicon carbides was similar. The first explosive event generated a total tangential strain of -0.06, and the second explosive event provided a total tangential strain of -0.23. During the first explosive event, the ratio between the shear-band strain (e_s) and the total strain (e_t) varied from 0.24 to 0.36. As shown in Table III, SiC-III exhibited the highest ratio e_s/e_t in the first explosive event. This did not manifest itself in the second explosive event. During the second explosive event, shear localization produced approximately 55% of the total strain for all specimens.

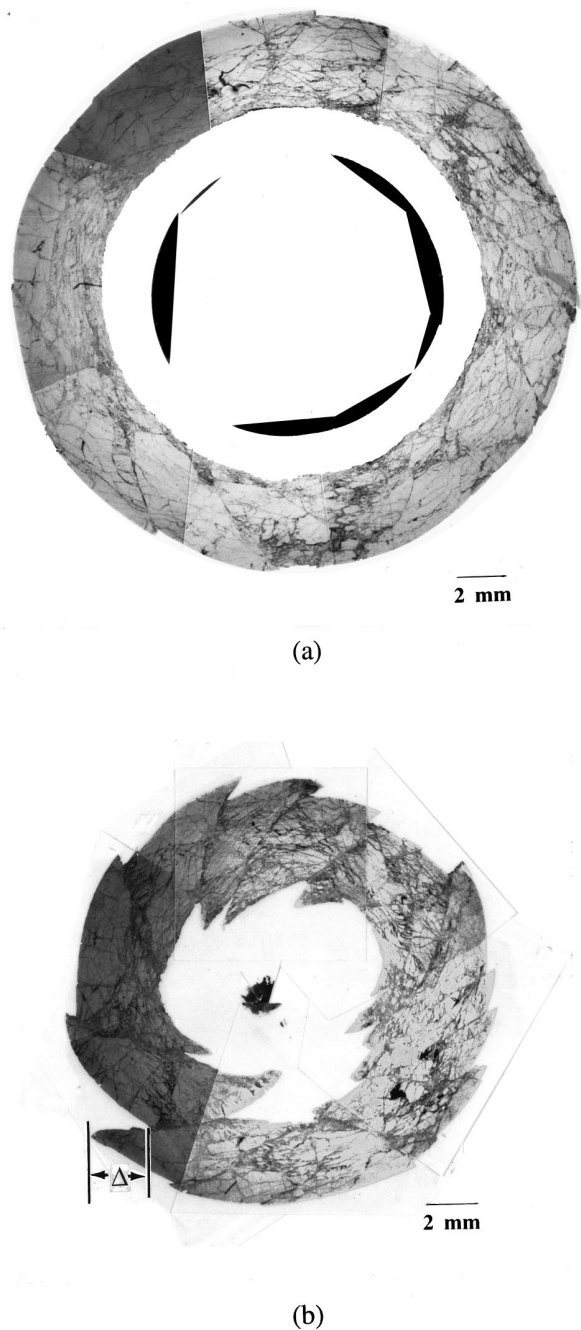J. Appl. Phys., Vol. 83, No. 9, 1 May 1998 Shih, Nesterenko, and Meyers

(a)

(b)

FIG. 3. Overview of ceramic specimens: (a) after the first explosive event, fragmentation, and (b) after the second explosive event, deformation.

Table IV summarizes the final configurations of all eight specimens after the second explosive event. The average shear-band spacing (S) is estimated from the total number of shear bands (N): $S = 2\pi r_m/\sqrt{2}N$, where r_m is the mean ra-

dius. There are two groups of shear bands: clockwise and counterclockwise. These two groups have roughly the same number of shear bands, and they occupy opposite sides of the cylinder. This grouping of shear bands into clockwise or counterclockwise is indicative of cooperative material motion and self-organization among the bands.

The trajectories of the incipient shear bands have been mathematically expressed by Nesterenko et al.[24] It is assumed that shear bands are formed along directions making 45° with the radial directions, corresponding to the surfaces of the maximum shear stress. The shear bands initiate at the regions of highest strain (close to the inner radius of the ceramic cylinder) and propagate towards the external walls, with the tips following a trajectory of maximum shear stress. As deformation proceeds beyond the formation of shear bands, the shear-band displacement (Δ in Fig. 3) increases by the relative motion of adjacent blocks. During this process, it is necessary to rotate these fragmented blocks. Therefore, the symmetry of the deformation is broken and the state of pure shear is destroyed. As a result, the shear bands do not follow exactly the 45° directions at the end of the deformation. The trajectories of the shear bands at the end of the deformation can be expressed analytically by projecting the original 45° shear bands onto the final dimension:

$$\theta = \frac{1}{2} \ln \frac{r^2 + R_0^2}{r_{if}^2 + R_0^2}, \tag{5}$$

where θ and r are the polar coordinates ($\theta = 0$ at $r = r_{if}$), R_0 is the radius of the orifice ($R_0 = 5.5$ mm), and r_{if} is the final inner radius after the second explosive event.

The trajectories were calculated and 14 shear bands were used in the calculation: seven clockwise and seven counterclockwise, as shown in Fig. 4. The calculated trajectories are in good agreement with the experimental observations. However, the shear-band displacement is not represented in this simulation.

A. Cracks during the first explosive event

As shown in Fig. 5(a), numerous shear cracks were developed during the first fragmentation explosion. Shear cracks roughly followed directions 45° to the radial direction; cracks along 90° of the radial direction were also observed. The latter cracks are related to the release stress waves. As shown in Fig. 5(b), material comminution can be identified around the cracks.

An average fragment size can be established by the linear intercept method and was measured using optical microscopy at 50×. However, a better estimate of damage is the

TABLE II. Deformation during the first explosive event.

	$e_{\varphi\varphi}$ At inner radius	$e_{\varphi\varphi}$ At outer radius	Average No. of bands	$\Sigma\Delta$ mm	e_t	e_s	e_s/e_t
SiC-I	−0.093	−0.039	11	1.24	−0.062	−0.015	0.24
SiC-II	−0.090	−0.030	13	1.27	−0.058	−0.015	0.26
SiC-III	−0.093	−0.037	14	1.83	−0.060	−0.022	0.36

TABLE III. Deformation during the second explosive event.

	$e_{\varphi\varphi}$ At inner radius	$e_{\varphi\varphi}$ At outer radius	Average No. of bands	$\Sigma\Delta$ mm	e_t	e_s	e_s/e_t
SiC-I	-0.358	-0.138	10	9.52	-0.227	-0.120	0.53
SiC-II	-0.376	-0.127	16	10.59	-0.228	-0.133	0.58
SiC-III	-0.392	-0.136	13	10.00	-0.239	-0.126	0.53

crack surface area per unit volume (S_v), which is directly related to the mean linear intercept ($\bar{L}$),[25]

$$S_v = \frac{4}{\bar{L}}. \qquad (6)$$

The value is multiplied by 2 from Ref. 25 because one crack generates two surfaces. As shown in Table V, different SiC had different crack surface areas. SiC-I has the highest crack surface area. Since all specimens are tested under identical conditions, the difference in crack surface area is directly related to the intrinsic material properties. Consistently, SiC-I has a lower fracture toughness than SiC-II and SiC-III. Thus, the material with a lower fracture toughness has a higher crack surface area during the fragmentation explosive event.

B. Microstructure of shear bands

After the second explosive event, shear bands were fully developed. Many shear bands exhibited two adjacent cracks, as shown in Fig. 6(a). All shear bands contained numerous fragments, with a bimodal size distribution. The large fragments ranged from 20 to 200 μm, and the small fragments were less than, or equal to, the initial grain size (5.6 μm for SiC-I and 4.1 μm for SiC-II and SiC-III). These large fragments did not have sharp corners and contained numerous microcracks, as shown in Fig. 6(b). Just outside the shear bands, small particles and fragments can be identified, as shown in Fig. 6(c). These fragments also had the same characteristics as the large fragments inside the shear band: round corners and microcracks.

The maximum thickness of shear bands for SiC-I (200 μm) was lower than the one for SiC-II (350 μm) and SiC-III (400 μm); the average thickness was also lower for SiC-I (110 μm) than for SiC-II (170 μm) and SiC-III (150 μm). The localized shear strain inside the shear band (γ_s) can be estimated from the following equation:

$$\gamma_s = \frac{\Delta}{T}, \qquad (7)$$

where Δ is the displacement of the shear band, and T is its thickness. This localized shear strain varied from 2 to 14, and the average of the localized shear strains were 7.1, 5.5, and 5.4, for SiC-I, SiC-II, and SiC-III, respectively.

C. Microstructure outside the shear bands

All three materials had extensive cracking outside the shear bands. In general, the cracks were along the $\pm45°$ and 90° directions to the radial direction. These orientations were identical to the ones after the first explosive event.

With respect to the interaction between the cracks and microstructure, SiC-II and SiC-III had a predominantly intergranular fracture mode and SiC-I tended to fracture in a transgranular pattern, as shown in Fig. 7. This is consistent with the results of quasistatic testing, as shown in Fig. 1. Therefore, it is concluded that the materials with segregated grain boundaries exhibit intergranular fracture, regardless of strain rate. As a result, the cracks in SiC-II and SiC-III were tortuous and the cracks in SiC-I were straight. In SiC-II and SiC-III, material comminution was often observed around the cracks, but SiC-I had less comminution under the same situation. It is obvious that the microstructural differences affect the roughness of the crack surfaces, resulting in differences in comminution, shear-band thickness, and localized shear strain. However, the overall macroscopic deformation is not influenced by the microstructure, as shown in Tables II and III.

D. Mechanism for shear-band formation

The spacing of the shear bands defines blocks of material that exhibit large relative translation. The treatment by Grady and Kipp[26] is based on the assumption that the kinetic and strain energies of the material prior to fragmentation can

TABLE IV. Summary of shear-band configurations of SiC.

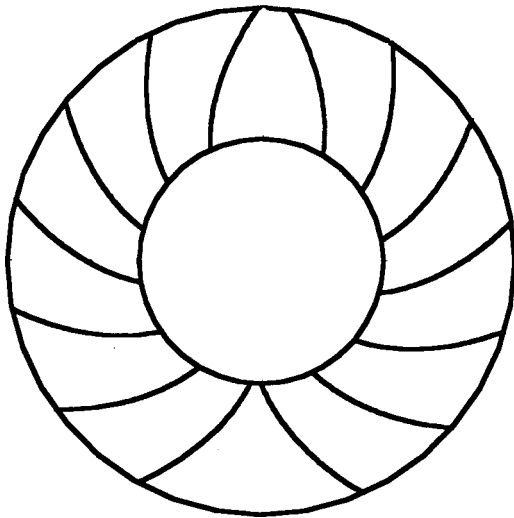|	Specimen No.	No. of groups	No. of shear bands	Average shear-band spacing	Average displacement
SiC-I	1	2	11	2.81 mm	0.904 mm
	2	2	10	3.05 mm	0.910 mm
SiC-II	1	2	18	1.72 mm	0.548 mm
	2	2	17	1.73 mm	0.561 mm
	3	2	14	2.18 mm	0.884 mm
SiC-III	1	2	15	2.02 mm	0.669 mm
	2	2	11	2.75 mm	0.907 mm

FIG. 4. Calculated shear-band trajectories.

(a)

(b)

FIG. 5. Microstructure of cracks after the first explosive event: (a) overview, and (b) high magnification showing material comminution along crack surfaces.

be equated to the energy required to produce the cracks. This analysis enables the prediction of the fragment size (L) using the material resistance to crack propagation (toughness K_c), density (ρ), sonic velocity (C), and strain rate ($\dot{\epsilon}$):

$$L = \left(\frac{\sqrt{24} K_c}{\rho C \dot{\epsilon}} \right)^{2/3}. \tag{8}$$

This equation shows that the fragment size increases with the material resistance to cracking and decreases with strain rate. This relationship can be extended to shear-band spacing, and provides important qualitative trends. The material parameters for silicon carbide are known: $\rho = 3.2 \times 10^3$ kg/m^3, and $C = 12 \times 10^3$ m/s; the experimental procedure yields $\dot{\epsilon} = 3 \times 10^4$ s^{-1}. It is instructive to apply this equation to the configuration investigated here. Figure 8 shows the relationship between the fragment size (L) and toughness (K_c). The material parameters need some modifications for this thick-walled cylinder experiment. For example, the ceramics have been prefractured in the first explosive event, and the fracture toughness, density, and the sonic velocity would be different from the ones of the as-pressed material. The toughness, or resistance of the material to flow in shear, is also dependent on the superimposed compressive stresses, which affect the friction. The shear localization occurs by mode II (or mixed mode I and II) loading, rather than a pure mode I loading. The toughness K_c should be replaced by the mode II fracture toughness (K_{IIC}). Shetty and co-workers[27,28] propose that K_{IIC} is not an intrinsic material property, and that there is no unique relationship between K_{IIC} and K_{IC}. However, experiments show that K_{IIC} of ceramics varies between 0.7 and 2 K_{IC}.[29,30] Polycrystalline ceramics seem to exhibit significantly higher normalized mode II fracture toughness, as compared with glasses, because of grain interlocking and abrasion.[30] Furthermore, Suresh et al.,[31] Brockenbough et al.,[32] and Freund[33] have shown that the K_{IC} increases with strain rate. It is anticipated that the K_{IIC} is also influenced by the strain rate. For example, Nakano et al.[34] have demonstrated that when the stress intensity rate ($\dot{K}$) increases from 0.02 to
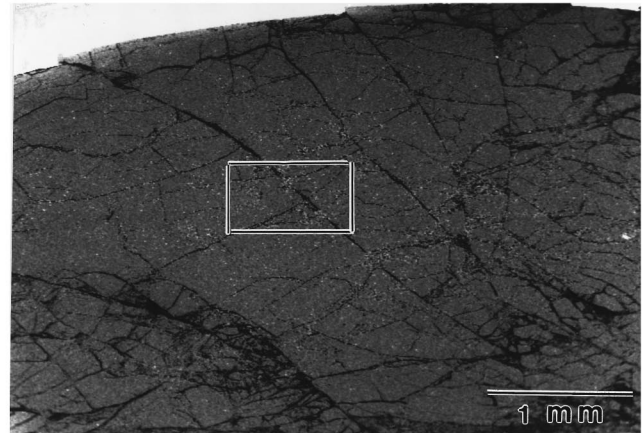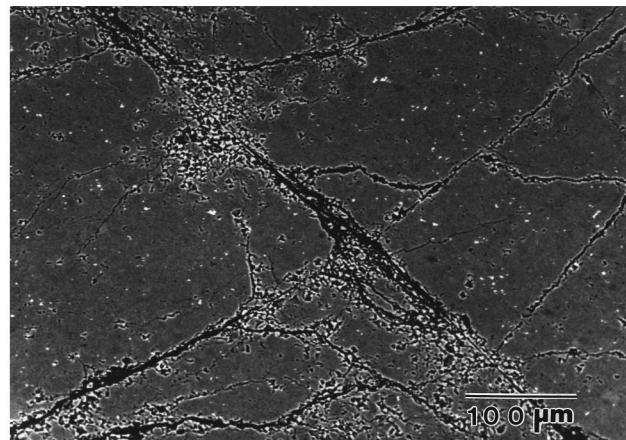
10^5 MPa$\sqrt{m}/s$, both K_{IC} and K_{IIC} of glasses increase twofold; however, Al$_2$O$_3$ has K_{IC} and K_{IIC} of 3.5 and 7.5 MPa$\sqrt{m}$, respectively, regardless of the strain rate.

This high-strain-rate experiment involves various complex situations, such as fragmented ceramics and mode II fracture. There is considerable uncertainty in the resistance of SiC to shear at the imposed strain rate. As shown in Fig. 8, the observed shear-band spacing (about 2.3 mm) corresponds to a toughness of 25 MPa$\sqrt{m}$, higher by a factor of

TABLE V. Crack surface area after the first explosive event.

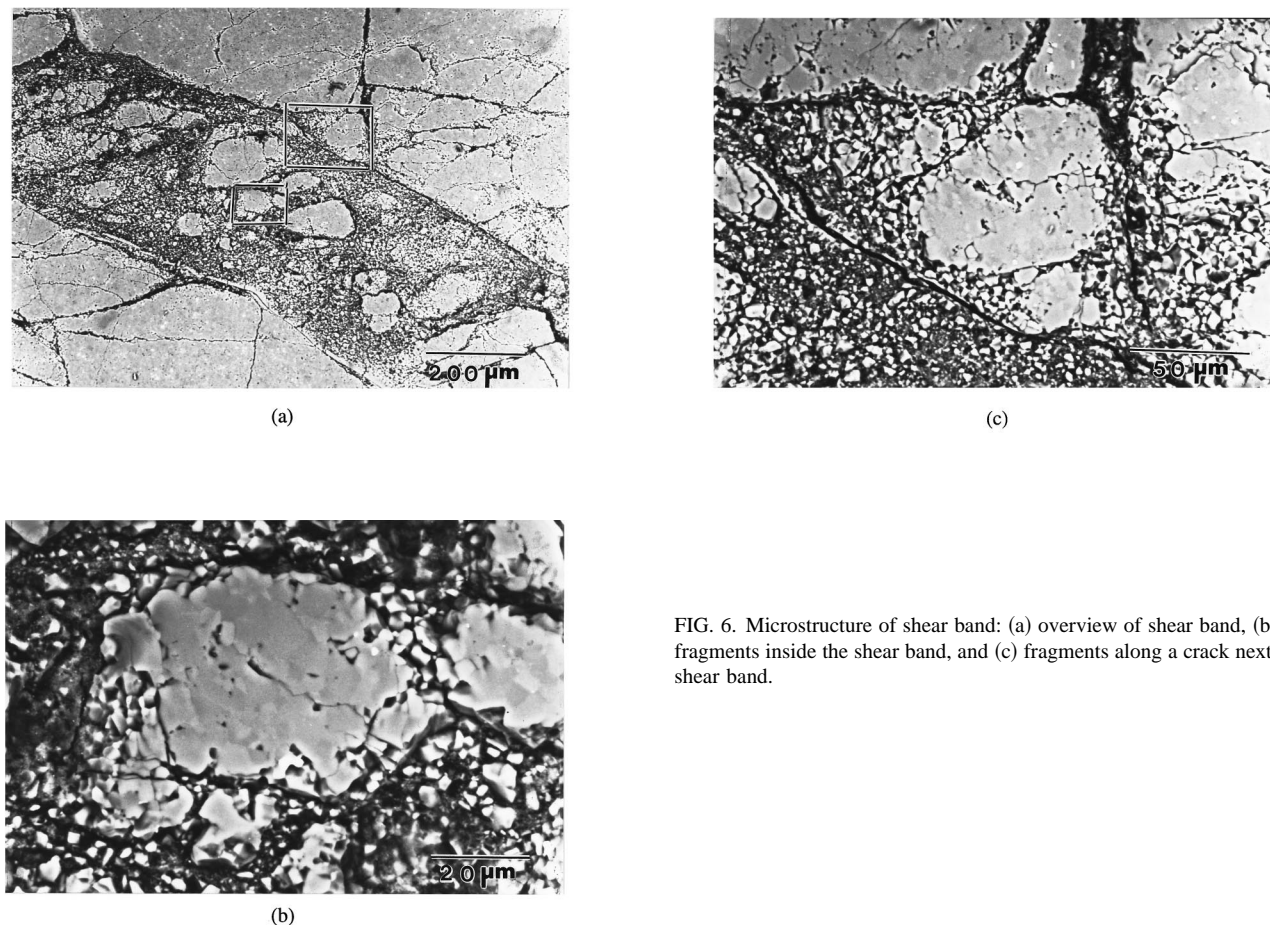|	S_v mm^2/mm^3
SiC-I	41.2±2.0
SiC-II	29.0±1.6
SiC-III	31.8±1.2

FIG. 6. Microstructure of shear band: (a) overview of shear band, (b) large fragments inside the shear band, and (c) fragments along a crack next to the shear band.

10 than K_{IC} for SiC $(2.5–4.3 \text{ MPa}\sqrt{m})$. The superimposed compressive stress for the experimental method is about 0.1 GPa. Equation (8) provides important qualitative trends, such as the effects of strain rate and resistance to shear. It will be shown in a later paper[35] that in granular SiC the shear-band spacing is considerably lower (0.5–1.2 mm, depending on the particle size). The same effects were observed for pre-fractured and granular Al_2O_3.[12,23] The average shear-band spacing for the prefractured Al_2O_3 is 2.0 mm, and the spacing is 0.49 and 0.61 mm for the granular Al_2O_3 with 0.4 and 4 μm particle size, respectively. One can state that the shear-band spacing is a characteristic scale that is governed by the release of elastic energy stored in the collapsing cylinder. The granular material, with a lower resistance to shear flow has a lower shear-band spacing in agreement with Eq. (8).

The flow of ceramics under dynamic loading is much less understood than that of metals, which has been extensively investigated.[36] In granular Al_2O_3, Nesterenko et al.[12] observed shear localization, which is due to a softening mechanism, not directly attributed to thermal effects. Shear localization in granular or fragmented materials can be rationalized as a mechanism to bypass the necessity of dilatation, which accompanies large inelastic deformation. Under small or no confinement, the deformation of a fragmented ceramic will exhibit dilatation. Curran et al.[7] developed a micromechanical model using two-dimensional square blocks with voids and dislocation arrays. The deformation of fragmented

materials is carried out through the sliding of the square blocks. Hegemier[37] proposed a hexagonal network of fragments to represent a fractured ceramic, as shown in Fig. 9(a). Hegemier's approach is used here to model dilatation. Upon deformation, the hexagonal fragments move with respect to each other to open the crack surfaces. As shown in Fig. 9(b), the volumetric dilatation (ratio of the void volume to the solid volume) can be represented by the areal ratio between the dashed parallelogram and the hexagon:

$$\delta = \frac{A_{\text{parallelogram}}}{A_{\text{hexagon}}} = \frac{4}{3\sqrt{3}} \frac{\chi}{D}, \qquad (9)$$

where D is the diagonal length of the hexagonal fragment, and χ is the height of the parallelogram. In an idealized configuration used here, the hexagons move along the direction 60° of the x axis. The volumetric dilatation can be related to the global shear strain γ:
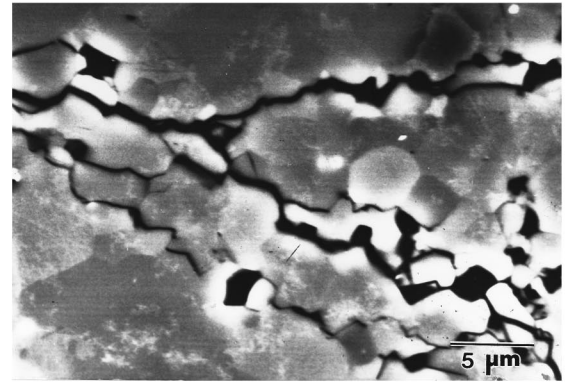
$$\delta = \frac{2\sqrt{3}}{3} \frac{\tan \gamma}{1 - \sqrt{3} \tan \gamma}. \qquad (10)$$

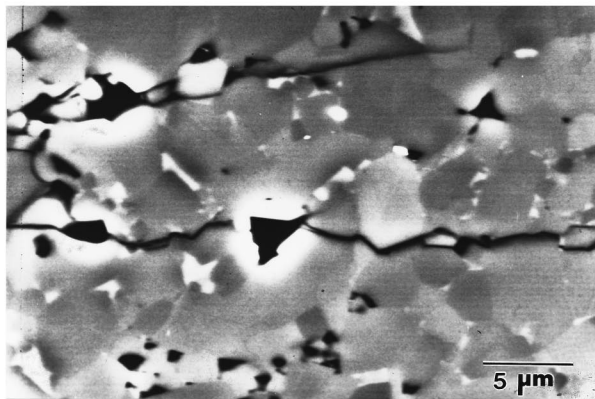As the deformation continues, the dilatation increases approximately linearly with strain. The dilatation reaches a

(a)

(c)
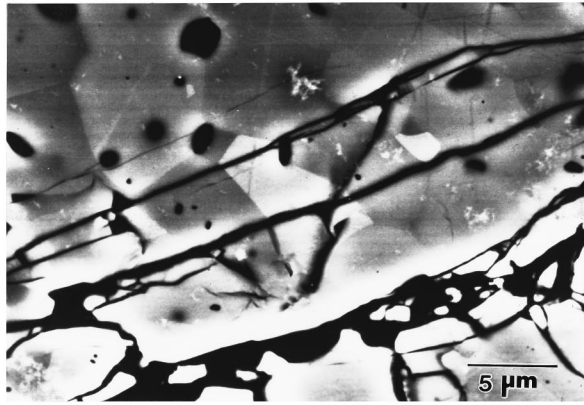
FIG. 7. Microstructure/crack interaction outside the shear band: (a) SiC-I: transgranular, (b) SiC-II: intergranular, and (c) SiC-III: intergranular.

(b)

maximum at $\chi_{max} = (\sqrt{3}/4)D$, corresponding to $\tan \gamma = 1/3\sqrt{3}$, as shown in Fig. 9(c). After this critical condition, the hexagonal blocks move along the shear direction, leading to a decrease in dilatation, as shown in Fig. 9(d). The volumetric dilatation is then represented by the following equation, for $\gamma > \tan^{-1}(1/3\sqrt{3})$:
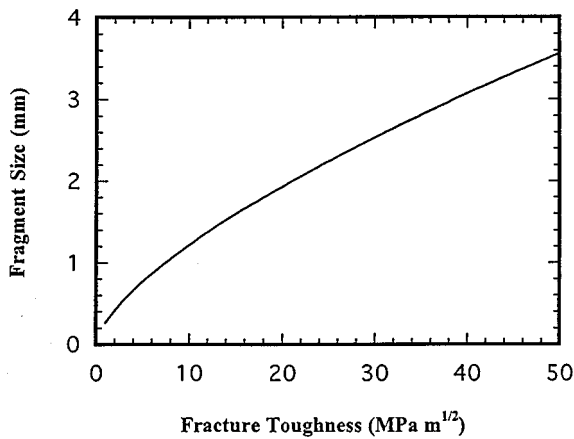

(a)   (b)

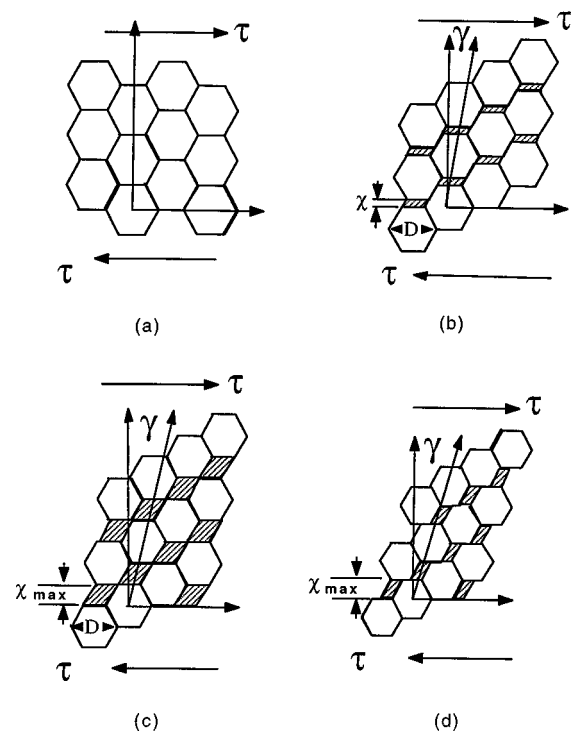

(c)   (d)

FIG. 9. Homogeneous deformation through Hegemier mechanism: (a) formation of hexagonal fragments, (b) crack opening and dilatation, (c) dilatation reaching its maximum, and (d) reduction in dilatation.
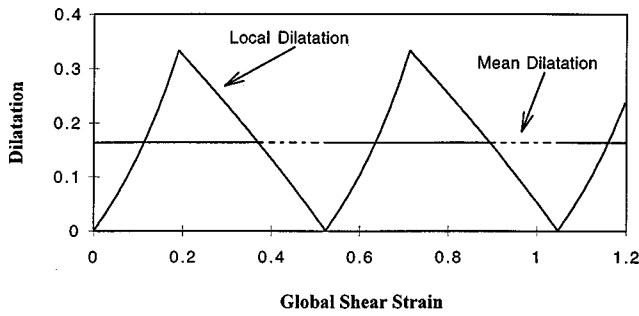

FIG. 8. Fragment size as a function of fracture toughness, using the Grady–Kipp relationship.

FIG. 10. Local and mean dilatation in the homogeneous deformation.

$$\delta = \frac{1}{2} - \frac{\sqrt{3}}{2} \tan \gamma. \qquad (11)$$

Further deformation will return the dilatation to zero because of the rearrangement of the hexagonal fragments. Figure 10 shows the change in dilatation with global shear strain. The dilatation increases with shear strain until reaching its maximum ($\delta_{max} = \frac{1}{3}$), and then gradually decreases to zero, at $\gamma = \pi/6$. Further shear deformation would repeat the dilatation cycle. In reality, not all fragments move along the same direction, and the overall dilatation would not have this simple periodical variation. By integrating the dilatation with respect to the strain, one can find the mean dilatation (δ_m) in this dilatation cycle:

$$\delta_m = \frac{\int_0^{\pi/6} \delta d\gamma}{\frac{\pi}{6}} = 0.16. \qquad (12)$$

This represents the mean dilatation in the two-dimensional deformation by the motion of hexagonal blocks with the same size.

With lateral confinement (superimposed compressive stresses), the dilatation is constrained, and the homogeneous deformation mechanism is inhibited. The sequence of the inhomogeneous deformation is shown in Fig. 11. A similar array of Hegemier hexagonal fragments is formed first. Material comminution occurs along a narrow band, which provides a path for shear; this comminution is initiated in some localized regions and propagates along a shear band. Further macroscopic deformation takes place through the extension and thickening of the shear band.

The total dilatation (δ_t) is determined by the dilatation inside the shear band (δ_s):

$$\delta_t = \delta_s \frac{T}{S}, \qquad (13)$$

where T is the shear-band thickness, and S is the shear-band spacing. In this inhomogeneous deformation process, the deformation is concentrated in the shear bands, and Hegemier's homogeneous mechanism is applicable inside the shear localization regions [see the detail in Fig. 11(b)], with a reduction of the scale of the unit hexagons. Therefore, one can consider a constant dilatation inside the shear band; i.e., $\delta_s = \delta_m = 0.16$. In our experiments, the average shear-band thickness is about 150 μm and the shear-band spacing is about 2.3 mm. Equation (13) predicts a total volumetric di-
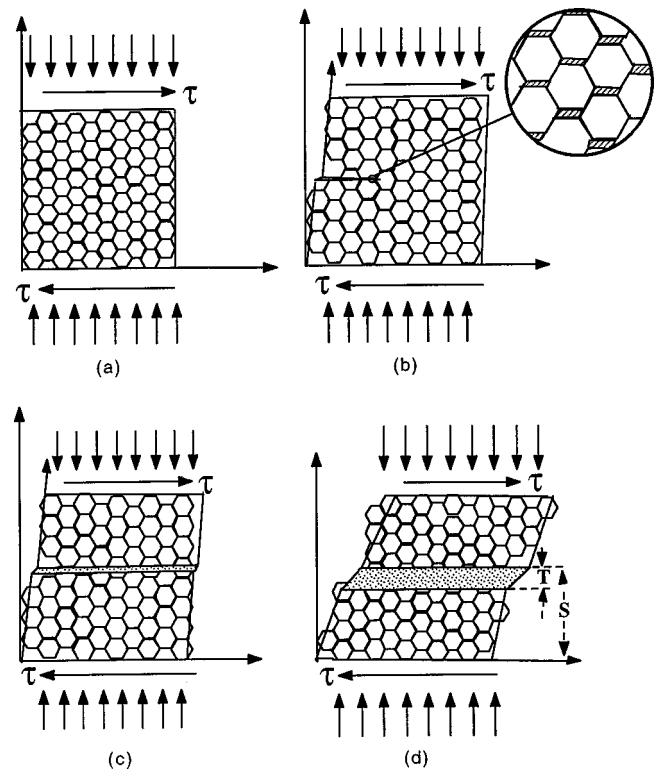

FIG. 11. Inhomogeneous deformation under high lateral confinement: (a) formation of hexagonal fragments, (b) initiation of shear band, (c) developed shear band, and (d) propagation of shear-band thickening.

latation of 0.01, which is much smaller than the dilatation associated with homogeneous deformation. It is clear that shear localization is a favorable deformation mechanism under constrained dilatation.

Based on the microstructural observations, the following mechanism is proposed for shear-band formation in SiC, as schematically depicted in Fig. 12:

(a) The material is first fragmented through the formation of cracks [Fig. 12(a)].

(b) Moderate comminution proceeds through the friction of crack surfaces, corresponding to the initiation of shear bands [Fig. 12(b)].

(c) When the two interfaces of the shear band start to move in opposite directions, the adjacent fragments are incorporated into the shear band [Fig. 12(c)].

(d) With further shear, these fragments are rotated and eroded in the shear band. The shear-band thickens through the continuous incorporation of fragments into the band and their erosion during flow [Fig. 12(d)].

Approximately 55% of the total tangential strain is accommodated by the shear localization, which is carried out by comminution, through incorporation and erosion of fragments. The micromechanical model of inelastic flow of comminuted ceramics proposed by Curran et al.[7] should be modified to include the effect of shear localization.

E. Bending effect

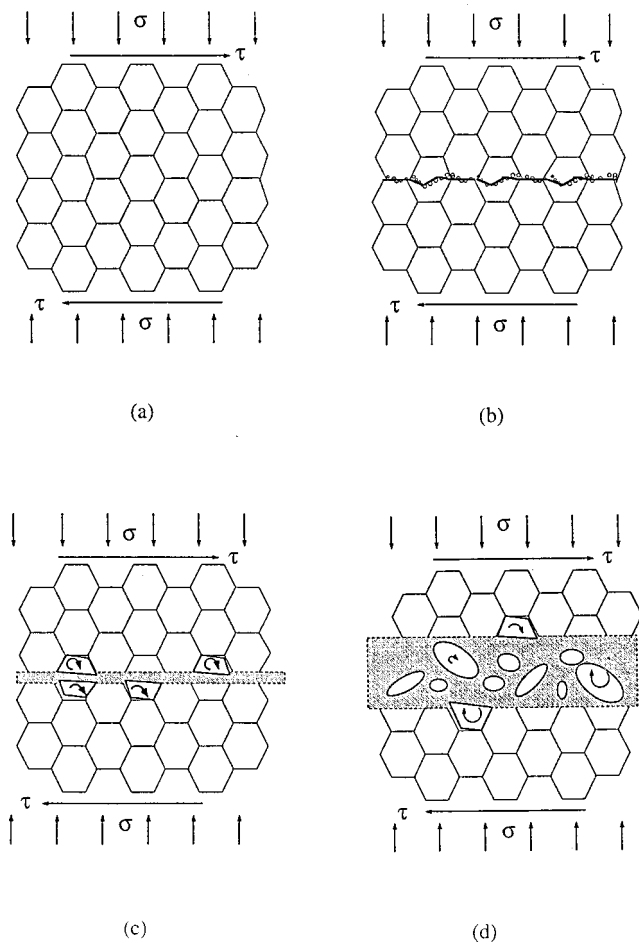Material comminution was also observed outside the shear bands through the advance of a comminution front by

FIG. 12. Schematic diagram for the mechanism for the shear-band formation: (a) fragmentation, (b) comminution along the crack surfaces, (c) incorporation of adjacent fragments, and (d) erosion of fragments and shear-band thickening.

FIG. 13. Comminution by local bending: (a) overview, and (b) high magnification at the comminution front.

localized bending, as shown in Fig. 13(a). This comminution front clearly defines a boundary between the comminuted region and the fragmented area, as shown in Fig. 13(b).

A schematic representation is shown in Fig. 14. A shear band separates two fragmented blocks, and the size of the blocks is determined by the spacing of the shear bands. During shear-band propagation, the shear displacement increases accordingly. However, these two blocks cannot keep the same orientation during the large deformation. Their rotation is necessary to accommodate the translation along the shear surfaces. A localized bending is, therefore, induced to alter the shape and orientation of these two fragmented blocks. Material comminution is the deformation mechanism that accomplishes the alteration of the geometry of the fragmented blocks. During this localized bending, a comminution front is initiated in the inner radius region and propagates towards the outer radius region. Comparing Fig. 13 with Fig. 6, one can observe that the fraction of material comminution outside shear bands by bending is much less than the fraction of comminution inside the shear bands. Therefore, bending comminution is considered as a secondary comminution mechanism.

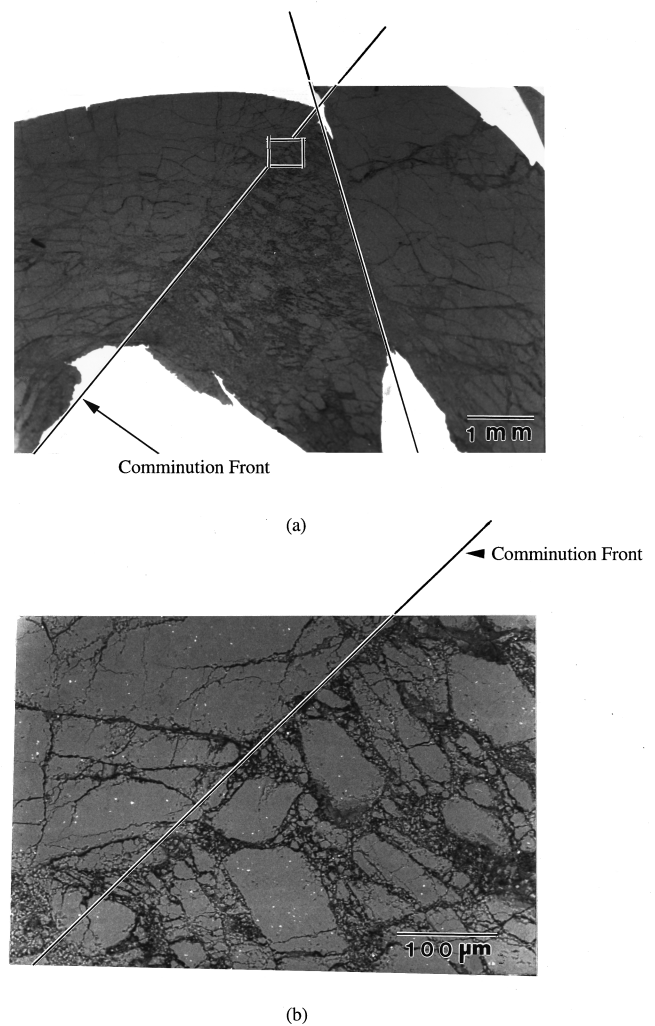In summary, the shear-band spacing introduces a new scale in fragmented materials: the size of fragmented blocks.

The material movement outside the shear localization bands can be considered mainly as the deformation within the fragmented blocks. This deformation is carried out by comminution, through propagating comminution fronts.

IV. CONCLUSIONS

(1) Controlled experiments on prefragmented silicon carbide have demonstrated that microstructural differences that affect the grain-boundary strength have little effect on the overall response to high-strain, high-strain-rate deformation. It should be emphasized that these silicon carbides have approximately the same grain size $(4–6\ \mu m)$ and that only kinematical observations were made. The stress levels at which the phenomena occurred were not measured and could very well differ substantially, in accordance with the strength and toughness differences of the three conditions.

(2) In large strain, high-strain-rate deformation of prefractured silicon carbide, shear localization plays an important role. Approximately 55% of the total tangential strain is accommodated inside shear localization regions.
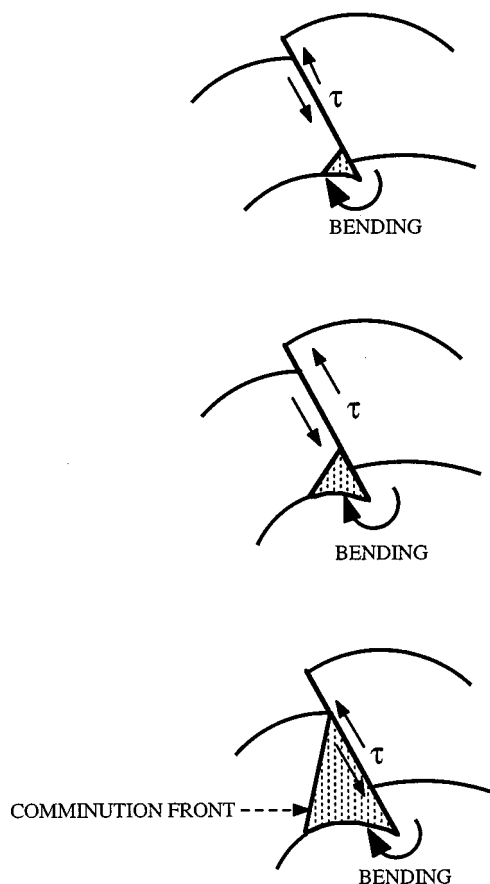
FIG. 14. Schematic diagram showing the comminution by local bending.

The spacing of shear bands is approximately the same for all three conditions (≈ 2.3 mm). Grady and Kipp's[26] energetic analysis of fragment size was applied to the prediction of shear-band spacings.

(3) Microstructural differences affect the microcrack propagation path: the materials with segregated grain boundaries (SiC-II and SiC-III) exhibit intergranular cracks, while SiC-I exhibits transgranular fracture. This type of microstructure/crack interaction is independent of strain rate.

(4) The development of shear bands occurs through: (a) shear crack formation, (b) rubble formation through friction of crack surfaces, (c) incorporation of adjacent fragments into the shear band, and (d) erosion of large fragments inside the shear band. The thickness of shear bands increases with global strain.

(5) In addition to the comminution of material taking place inside the shear bands, the formation of comminution regions due to bending has also been observed. During the propagation of shear bands, bending comminution is essential to alter the orientation of the fragmented blocks. This bending comminution also increases with global strain.

ACKNOWLEDGMENTS

[1] D. Viechnicki, W. Blumenthal, M. Slavin, C. Tracy, and H. Skeele, Armor ceramics—1987, Proceedings of the Third TACOM Armor Coordinating Conference, 17–19 February 1987, Monterey, California (1987).

[2] D. J. Viechnicki, M. J. Slavin, and M. I. Kliman, Ceram. Bull. **70**, 1035 (1991).

[3] D. A. Shockey, A. K. Marchaud, S. R. Skaggs, G. E. Corte, M. W. Burkett, and R. Parker, Int. J. Impact Eng. **9**, 263 (1990).

[4] M. A. Meyers, *Dynamic Behavior of Materials* (Wiley, New York, 1994), p. 597.

[5] G. E. Hauver, P. H. Netherwood, R. F. Benck, and L. J. Kecskes, Proceedings of the 13th Army Symposium on Solid Mechanics, p. 23 (1993).

[6] G. E. Hauver, P. H. Netherwood, R. F. Benck, and L. J. Kecskes, Proceedings of 19th Army Science Conference, p. 1 (1994).

[7] D. R. Curran, L. Seaman, T. Cooper, and D. A. Shockey, Int. J. Impact Eng. **13**, 53 (1993).

[8] R. W. Klopp and D. A. Shockey, J. Appl. Phys. **70**, 7318 (1991).

[9] S. Sairam and R. J. Clifton, Mechanical Testing of Ceramics and Ceramic Composites, AMD Vol. 197 (ASME, New York, 1996), p. 23.

[10] R. W. Klopp, D. A. Shockey, L. Seaman, D. R. Curran, J. T. McGinn, and T. Resseguier, Mechanical Testing of Ceramics and Ceramic Composites, AMD Vol. 197, (ASME, New York, 1996), p. 41.

[11] W. Chen and G. Ravichandran, J. Mech. Phys. Solids **45**, 1303 (1997).

[12] V. F. Nesterenko, M. A. Meyers, and H. C. Chen, Acta Mater. **44**, 2017 (1996).

[13] R. Telle, *Materials Science and Technology*, Vol. 11, Structure and Properties of Ceramics (VCH, Weinheim, 1994), p. 173.

[14] M. Srinivasan, Structural Ceramics, Treatise on Materials Science and Technology, Vol. 29, p. 99 (1989).

[15] A. Ezis, Monolithic, Fully Dense Silicon Carbide Mirror and Method of Manufacturing, U.S. Patent, No. 5,302,561 (1994).

[16] T. Watanabe, Mater. Sci. Eng. A **176**, 39 (1994).

[17] R. H. Jones, C. H. Schilling, and L. H. Schoenlein, Mater. Sci. Forum **46**, 277 (1989).

[18] D. G. Munz, J. L. Shannon, and R. T. Bubsey, Int. J. Fract. **16**, R137 (1980).

[19] C. A. Johnson and W. T. Tucker, *Engineered Materials Handbook*, Vol. 4, Ceramics and Glasses (ASM International, Metals Park, OH, 1991), p. 709.

[20] M. P. Bondar and V. F. Nesterenko, J. Phys. IV **1**, 163 (1991).

[21] V. F. Nesterenko and M. P. Bondar, Dymat J. **1**, 245 (1994).

[22] V. F. Nesterenko, M. A. Meyers, H. C. Chen, and J. C. LaSalvia, Metall. Mater. Trans. A **26A**, 2511 (1995).

[23] H. C. Chen, M. A. Meyers, and V. F. Nesterenko, in *Shock Compression of Condensed Matter* (AIP Press, New York, 1995), p. 607.

[24] V. F. Nesterenko, M. A. Meyers, and T. W. Wright, in *Metallurgical and Materials Applications of Shock Wave and High-Strain-Rate Phenomena* (Elsevier Science, New York, 1995), p. 397.

[25] M. A. Meyers and K. K. Chawla, in *Mechanical Metallurgy* (Prentice-Hill, Englewood Cliffs, NJ, 1984), p. 497.

[26] D. E. Grady and M. E. Kipp, Int. J. Rock Mech. Min. Sci. **17**, 147 (1980).

[27] D. K. Shetty, J. Eng. Gas Turbines Power **109**, 282 (1987).

[28] D. K. Shetty, A. R. Rosenfield, and W. H. Duckworth, J. Am. Ceram. Soc. **69**, 437 (1986).

[29] V. Tikare and S. R. Choi, J. Am. Ceram. Soc. **76**, 2265 (1993).

[30] D. Singh and D. K. Shetty, J. Am. Ceram. Soc. **72**, 78 (1989).

[31] S. Suresh, T. Nakamura, Y. Yeshurun, K.-H. Yang, and J. Duffy, J. Am. Ceram. Soc. **73**, 2457 (1990).

[32] J. R. Brockenbrough, S. Suresh, and J. Duffy, Philos. Mag. **58**, 619 (1988).

[33] L. B. Freund, *Dynamic Fracture Mechanics* (Cambridge University Press, Cambridge, 1990).

[34] M. Nakano, K. Kishida, Y. Yamauchi, and Y. Sogabe, J. Phys. IV **C8**, 695 (1994).

[35] C. J. Shih, V. F. Nesterenko, and M. A. Meyers, Acta. Mater. (in press).

[36] Y. Bai and B. Dodd, in *Adiabatic Shear Localization* (Pergamon, Oxford, 1992), p. 54.

[37] G. Hegemier, UCSD (private communication, 1991).